Published in final edited form as:

J Mol Biol. 2023 January 15; 435(1): 167710. doi:10.1016/j.jmb.2022.167710.

Membrane Binding Induces Distinct Structural Signatures in the Mouse Complexin-1C-Terminal Domain

Emily M. Grasso[1], **Mayu S. Terakawa**[1], **Alex L. Lai**[2], **Ying Xue Xie**[1], **Trudy F. Ramlall**[1], **Jack H. Freed**[2], **David Eliezer**[1]

[1] -Department of Biochemistry, Weill Cornell Medicine, New York, NY, United States

[2] -Department of Chemistry and Chemical Biology, Cornell University, Ithaca, NY, United States

Abstract

Complexins play a critical role in regulating SNARE-mediated exocytosis of synaptic vesicles. Evolutionary divergences in complexin function have complicated our understanding of the role these proteins play in inhibiting the spontaneous fusion of vesicles. Previous structural and functional characterizations of worm and mouse complexins have indicated the membrane curvature-sensing C-terminal domain of these proteins is responsible for differences in inhibitory function. We have characterized the structure and dynamics of the mCpx1 CTD in the absence and presence of membranes and membrane mimetics using NMR, ESR, and optical spectroscopies. In the absence of lipids, the mCpx1 CTD features a short helix near its N-terminus and is otherwise disordered. In the presence of micelles and small unilamellar vesicles, the mCpx1 CTD forms a discontinuous helical structure in its C-terminal 20 amino acids, with no preference for specific lipid compositions. In contrast, the mCpx1 CTD shows distinct compositional preferences in its interactions with large unilamellar vesicles. These studies identify structural divergences in the mCpx1 CTD relative to the wCpx1 CTD in regions that are known to be critical to the wCpx1 CTD's role in inhibiting spontaneous fusion of synaptic vesicles, suggesting a potential structural basis for evolutionary divergences in complexin function.[1]

Keywords

Synaptic vesicle trafficking; SNARE-mediated exocytosis regulation; Protein:vesicle interactions; Curvature sensitivity; Disorder-to-order transition

Accession Numbers

mCpx1 CTD BMRB ID: **51396**. mCpx1 CTD + DPC micelles BMRB ID: **51397**.

CRediT authorship contribution statement

Emily M. Grasso: Conceptualization, Methodology, Formal analysis, Investigation, Writing – original draft, Writing – review & editing, Visualization. **Mayu S. Terakawa:** Conceptualization, Methodology, Investigation. **Alex L. Lai:** Methodology, Formal analysis, Investigation, Writing – review & editing. **Ying Xue Xie:** Methodology, Investigation. **Trudy F. Ramlall:** Methodology, Investigation. **Jack H. Freed:** Conceptualization, Methodology, Writing – review & editing, Supervision, Funding acquisition. **David Eliezer:** Conceptualization, Methodology, Writing – review & editing, Supervision, Funding acquisition.

Appendix A. Supplementary Data

Supplementary data to this article can be found online at https://doi.org/10.1016/j.jmb.2022.167710.

Introduction

SNARE-mediated exocytosis of synaptic vesicles (SVs) is essential to the transmission of chemical signals in neurons.[1–3] This process is tightly regulated by a number of proteins both to facilitate evoked exocytosis in response to the proper stimuli and to limit spontaneous exocytosis in the absence of such stimuli.[4–5] Complexins are a family of proteins critical for regulating both spontaneous and calcium-mediated evoked SV exocytosis.[3,6–10] Partial knock-outs and mutations in complexins induce neurological defects and reduce lifespan in mammals,[10–14] highlighting the centrality of complexins to proper SV release. The excitatory function of complexin is well conserved throughout invertebrates and vertebrates, but significant controversy remains over its inhibitory role.[15–16] Invertebrate complexins strongly inhibit spontaneous fusion of SVs with the plasma membrane,[17–19] but this effect is much weaker or absent in mammals,[20–22] leaving lingering questions about the mechanistic origins of these evolutionary divergences.

Studies of the structural and functional features of various complexins have established that these proteins, though small, can be subdivided into four domains that play different roles in regulating SV exocytosis (Figure 1(A–B)).[15,20] The N-terminal domain (NTD) is unstructured in solution and thought to play a significant role in Ca^{2+} evoked fusion in mammals,[23] but not in worms.[19] The subsequent accessory helical domain (AHD) contributes to inhibition of vesicle release and is highly helical even in the absence of binding partners in all complexins. This structure has been proposed to nucleate helicity in the central helix domain (CHD),[24–25] which binds to the SNARE proteins synaptobrevin and syntaxin,[24–28] or to interfere in SNARE mediated fusion via other mechanisms.[29–33] The CHD is essential for both the inhibitory and excitatory functions of complexins. Finally, the C-terminal domain (CTD) is intrinsically disordered (ID) and has been shown in both worm (*C. elegans*) and mouse (*M. musculus*) complexins to specifically interact with highly curved membranes.[34,35,66] The interactions between the CTD and membranes play a critical role in tethering complexin to SVs and are critical for the inhibitory function of complexin in worms.[36] Recent studies suggest a potential role for CTD-membrane interactions in the excitatory function of complexin as well.[37]

Previous studies have indicated that differences in the CTDs of mouse and worm complexins may be largely responsible for functional differences between the proteins.[36,38–40] The CTD of worm complexin 1 (wCpx1 CTD) has been extensively structurally characterized, revealing that the multiple sub-domains exist within the larger domain[34,41] (Figure 1(B)). Though largely disordered in the absence of membranes, a short helical structure (AH2) exists near the N-terminus of this region. The C-terminus of the domain interacts strongly with membranes via an amphipathic helix motif (AH-motif) and a subsequent C-terminal motif (CT-motif). The AH-motif forms an amphipathic helix only in the presence of highly curved membranes.[34,41] Similar AH-motifs have been annotated in the CTDs of non-worm complexins, suggesting this is a common structural motif conserved across evolutionary space.[35–36,42] The CT-motif remains unstructured even when bound to membranes. Both sub-domains are essential for inhibition of spontaneous SV fusion in worms.[36] Disrupting the AH-motif decreases membrane binding locally in that region, while removing the CT-motif abolishes membrane interactions of the CTD entirely.[34,36]

There are clear connections between the structural features of the wCpx1 CTD and its inhibitory function, but similar information on complexins from other organisms is lacking. The mouse complexin 1 (mCpx1) CTD has also been shown to interact strongly with highly curved membranes[34–35] and putative AH- and CT-motifs in the mCpx1 CTD have been defined (Figure 1 (C)). However, replacing the wCpx1 AH- or CT-motifs with the corresponding putative mCpx1 motifs does not restore inhibitory function in worms,[38] indicating a potential divergence of these structural motifs. A more thorough characterization of the structural features of the mCpx1 CTD is thus essential to understanding how it differs from invertebrate complexins.

Results

The C-terminal 20 residues of the mCpx1 CTD interact with lipid micelles

We first examined the mCpx1 CTD in the presence of dodecylphosphocholine (DPC) micelles, a membrane mimetic that was previously shown to recapitulate the structural features of the wCpx1 CTD bound to small unilamellar vesicles (SUVs).[34,41] This approach allowed us to apply solution nuclear magnetic resonance (NMR) spectroscopy, which would be less applicable when using SUVs due to their larger size and the associated broadening of NMR signals upon interactions with SUVs.

Comparison of 2D {^{15}N-^{1}H} HSQC spectra for free and DPC-bound mCpx1 CTD revealed that spectroscopic changes between the two states are limited to specific residues in the protein (Figure 2(A)). The majority of peaks in the spectra for free and micelle-bound mCpx1 CTD overlay extremely well, suggesting that large regions of the CTD are not interacting with the micelles in any significant capacity. To identify regions exhibiting changes in the presence of DPC, we completed NMR backbone resonance assignments (see methods) for the mCpx1 CTD in the absence and presence of DPC-micelles (Figure S1–2). Residues that are significantly affected by the presence of micelles all fall in the C-terminus of the CTD, specifically the terminal ~ 20 residues (114–134). These residues exhibit both chemical shift perturbations (CSPs) (Figure 2(B)) and attenuated signal intensities (Figure 2(C)) in the presence of micelles. Together, these data suggest that the C-terminus of the mCpx1 CTD is interacting with DPC-micelles while the N-terminal regions of the CTD are largely unaffected.

Both the AH- and CT-motifs form helical structure in the presence of DPC-micelles

Sequence analysis of the mCpx1 CTD defined putative AH- and CT-motifs in the C-terminus of the mCpx1 CTD similar to those characterized for wCpx1.[34,38,41] We previously reported that the last 6 amino acids of the mCpx1 CT-motif may form helical structure in the presence of lipids,[38] unlike the wCpx1 CT-motif, which remains unstructured even when bound to micelles.[34,38,41] Here we report a more thorough characterization, using a combination of circular dichroism (CD) and NMR spectroscopy, to define the structural features of the entire mCpx1 CTD in the absence and presence of micelles.

In the absence of lipids, the CD spectrum of the mCpx1 CTD is consistent with the protein being largely disordered in solution, but a slight decrease in signal around 220 nm that

indicates the unbound protein contains some helical structure (Figure 3(A)). Importantly, the mCpx1 CTD contains a single Tyr residue and a single Phe residue, making accurate protein concentration determination, and proper normalization of CD data, exceedingly difficult for this construct. Therefore, the CD data reported here are interpreted qualitatively. In the presence of DPC-micelles, the signal around 220 nm is more pronounced and the minimum observed for the free protein at 200 nm shifts to 205 nm. These changes are consistent with the micelle-bound CTD having a higher helical content than the unbound protein.

Using our NMR backbone resonance assignments for the free and DPC-bound protein, TALOS-N secondary structure predictions and ΔCα-ΔCβ calculations indicate that there is a substantial propensity for helical structure in a region encompassing approximately 10 residues (residue 76–86) near the N-terminus of the free CTD (Figure 3(B), Figure S3(A)). A similarly helical, though somewhat shorter, region was identified in the wCpx1 CTD and termed the amphipathic helix 2 (AH2) motif.[41] There is also a short stretch of amino acids around residue 120 (residues 120–124) that have a weak propensity for beta-strand structure, with unclear significance. The remainder of the CTD exhibits no significant secondary structure. In the presence of DPC-micelles, two distinct regions in the C-terminus of the mCpx1 CTD, encompassing residues 116–124 and 128–133, form stable helical structure (Figure 3(C), Figure S3(B–C)) that is not observed in the absence of micelles. The helical structure observed in the AH2-motif is unchanged in the presence of micelles.

To further assess the propensity for structure formation in the presence of DPC-micelles, we analyzed NH-NH NOEs from {^{1}H-^{15}N-^{1}H} (Figure 3(D)) and {^{15}N-^{15}N-^{1}H} (Figure 3E) NOESY experiments for the micelle-bound mCxp1 CTD. Residues spanning the regions from ~ 114–124 and 128–133 showed clear NH-NH NOEs from residue i to i ± 1, characteristic of helical structure, consistent with the regions defined as helical in the TALOS-N predictions. Residues 125–127 consist of Pro-Gly-Pro, precluding the observation of NH-NH i to i + 1 NOEs. However, this sequence is highly unfavorable for helical structure and likely represents a break between the two helices, as indicated by the chemical shift-based prediction.

These observations are further corroborated by ps-ns backbone relaxation data collected on both free and micelle-bound mCpx1 CTD. In the absence of micelles,^{15}N R_1 and R_2 measurements, along with heteronuclear {^{1}H-^{15}N} NOE (hetNOE) data are consistent with the protein being disordered in solution (Figure 4, S4). The ^{15}N R_1 and hetNOE data are fairly uniform across the length of the protein with slight decreases at the N- and C- termini and the values are consistent with a disordered protein at 10 °C (Figure 4, S4A). There are slight variations in the R_2 rates across the length of the protein, with field dependent increases in R_2 for the regions surrounding residues ~ 80 and ~ 120 that suggest these regions may experience a slight degree of restricted motions and/or chemical exchange in their free forms (Figure S4(B)).

In the presence of DPC micelles, there are notable changes in these ps-ns relaxation measurements. The R_1 data show a slight global decrease in relaxation rates for the micelle-bound protein relative to the free protein (Figure 4(A), S4 (C), S4E), though this is likely due to changes in temperature between free (10 °C) and micelle-bound (40 °C) data. Both

the R_2 and hetNOE data show significant changes in the presence of DPC micelles. R_2 rates for the terminal 20 residues of the mCpx1 CTD are significantly elevated relative to the free protein (Figure 4(B), S4(D), S4(F)); notably, the average R_2 relaxation rate (10.2 ± 1.2) for the residues encompassing the AH-motif (115–124) is higher than the average R_2 relaxation rate (8.5 ± 0.9) for the residues encompassing the CT-motif (128–133). Similarly, the hetNOE values for the terminal 20 residues of the mCpx1 CTD are elevated relative to the free form of the protein (Figure 4(C)). Notably, residues 125–127, constituting the non-helical PGP linker between the AH- and CT-motif helices, does not exhibit indications of increase mobility, suggesting that in the micelle-bound conformation, the linker conformation, while non-helical, may be relatively fixed.

Many of the peaks for the residues falling within the disordered regions of the micelle-bound CTD are not visible, likely due to rapid solvent exchange at the temperature at which the data were collected, but those that are visible are consistent with this region being highly disordered. Interestingly, the elevated R_2 values observed around position 80 in the unbound CTD disappear in the micelle-bound state. This could potentially reflect an intramolecular process involving the AH2-motif that is disrupted upon micelle binding. Together, the CD and NMR data clearly indicate that the mCpx1 CTD forms two distinct, relatively rigid helices at its C-terminus, corresponding to the AH- and CT-motifs, in the presence of DPC-micelles.

The mCpx1 AH- and CT-motifs interact with SUVs

With convincing evidence that helical structure forms in the C-terminus of the mCpx1 CTD in the presence of micelles, we sought to evaluate whether similar interactions occur with lipid bilayers in the form of small unilamellar vesicles (SUVs). We chose SUVs similar in size and charge to SVs, with which complexin interacts in cells. While the larger size of SUVs relative to micelles makes direct observation of SUV-bound proteins by NMR impracticable, NMR can still be used to detect and quantify SUV binding.

Comparison of 2D {^{15}N-^{1}H} HSQC spectra for the mCpx1 CTD free or bound to SUVs with two different lipid compositions (60% DOPC/25% DOPE/15% DOPS and 85% POPC/15% POPS) revealed significant attenuation of peak heights in the presence of SUVs (Figure 5(A)), without detectable chemical shift changes. There is a global decrease in signal intensity for all peaks in the SUV-bound spectra, but the C-terminal 20 residues show a greater decrease in intensity for both SUV compositions (Figure 5(B)) indicating that this region is interacting strongly with SUVs irrespective of their composition. The POPC/POPS data closely resemble preliminary data reported previously using the full-length mCpx1.[34]

The lack of chemical shift changes in the presence of SUVs indicates that the exchange of the mCpx1 CTD between its free and vesicle-bound states occurs in the slow-exchange limit on the NMR time scale. In this case, the relaxation rates of the protein in the bound state do not contribute significantly to the free state R_2 relaxation rate. Instead, assuming the interaction between the mCpx1 CTD and SUVs occurs on a similar time scale to that of R_2 relaxation of the free protein, the R_2 relaxation rates at sub-saturating SUV concentrations will be the sum of the free protein R_2 and the on rate for vesicle binding.[43] These experiments have previously been used to evaluate the association kinetics of worm

complexin,[34] as well as of the Parkinson's protein alpha-synucelin with lipids.[43] R_2 values for mCpx1 CTD at sub-saturating concentrations of SUVs composed of 60% DOPC/25% DOPE/15% DOPS and 85% POPC/15% POPS are elevated at the N- and C-termini relative to the free protein (Figure S5(A)). The change in R_2 is more pronounced at the C-terminus of the protein than the N-terminus (Figure S5(B)). These data corroborate an interaction between the C-terminus of the mCpx1 CTD and SUVs, as observed with DPC micelles. In contrast, the elevated R_2 rates at the N-terminus of the CTD in the presence of SUVs suggest this region, encompassing the AH2-motif, may be involved in interactions with SUVs that are not recapitulated in the micelle-bound state.

We next evaluated the secondary structure of SUV-bound mCpx1 CTD using CD spectroscopy. Challenges in accurate protein concentration determination, combined with increased noise due to light scattering from the SUVs, rendered CD analysis in the presence of SUVs highly challenging. Nevertheless, there are clear decreases in signal around 220 nm and shifts in the signal minimum from ~ 200 nm to ~ 205 nm for the SUV-bound CTD relative to the free protein (Figure 5(C)). Thus, the CD data are consistent with an increase in helical structure for the SUV-bound mCpx1 CTD relative to the free protein. Together, CD and NMR indicate that the terminal 20 amino acids of the mCpx1 CTD interact with SUVs and this binding is accompanied by an increase in helical structure.

ESR indicates two AH- and CT-motifs are helical in SUV-bound mCpx1

To further characterize the SUV-bound state of the mCpx1 CTD, we performed electron spin resonance (ESR) experiments using spin-labeled CTD in the presence of SUVs. These experiments provide residue-specific information about the local environment of the CTD, as well as distances between different sites. Spin labels were introduced by conjugation to single cysteine mutants in a cysteine-free (C105A) background. We collected continuous wave ESR (cwESR) power saturation data for mCpx1 CTD spin-labeled at each of the terminal 22 residues of the protein in the presence of SUVs composed of 60% DOPC/25% DOPE/15% DOPS and equilibrated with atmospheric oxygen or containing nickel(II) ethylenediaminediacetic acid (NiEDDA) and purged with nitrogen gas (see methods). By analyzing the partitioning of these spin-labels between O_2 and NiEDDA, we were able to evaluate the depth parameter, Phi, a measure of the relative accessibility of the residue to either the solvent or the membrane environment.

The ESR data revealed a periodic pattern of elevated partitioning to a membrane-like environment that is consistent with that expected for an amphipathic helix interacting with a membrane (Figure 6(A)). Fits to data from residues 113–134 to parameters consistent with a continuous alpha helical structure, using either a fixed or a floating periodicity, yielded poor R^2 values. Separately fitting the data in the AH-motif (residues 114–124, Figure 6(B)) and the CT-motif (residues 128–134, Figure 6(C)) yielded improved fits. Representing the sequence from residues 114–134 (Figure 6(A)) in a helical wheel format revealed an amphipathic distribution of residues, but residues F132 and K134 cross the boundary between the polar and apolar faces. Representing the AH- and CT-motif sequences separately (Figure 6(B,C)) yields two shorter amphipathic helices without violations. These data clearly demonstrate that the helical structure observed for the AH- and CT-motifs in

micelle-bound mCpx1 CTD is also present in the SUV-bound state. While there is no clear separation of the two regions in the cwESR data, two distinct helical motifs, as observed in the DPC micelle-bound state, fit the data somewhat better in its C-terminus.

We then analyzed the relative distances between different regions of the CTD in its micelle-bound and SUV-bound states using double electron–electron resonance (DEER) experiments. We used the native cysteine (C105) in the mCpx1 CTD, which is in a region that does not interact with membranes, and two positions in the C-terminus: I121C, which falls in the AH-motif, and F132C, which falls in the CT-motif. The average distance from C105 to I121C is 2.3 ± 0.2 nm in the presence of SUV and 2.3 ± 0.1 nm in the presence of DPC-micelles, indicating that the relative position of the AH-motif to C105 is likely similar in the presence of either micelles and SUVs (Figures S6(A, C and E)). In contrast, the average distance from C105 to F132C is 3.5 ± 0.1 nm in the presence of SUV and 4.3 ± 0.1 nm in the presence of DPC-micelles (Figures S6(B, D and E)). These data indicate that some aspect of the topology of the CTD, especially in the vicinity of the CT-motif, diverges in its SUV-bound state from the micelle-bound structure. In particular, the CT-motif is less co-linear with the AH-motif in the SUV-bound vs. micelle-bound state, supporting the idea that the two helical motifs are formed independently from each other and suggesting that the PGP sequence separating them may be flexible.

Fluorescence-based experiments corroborate two helical motifs in the presence of SUVs

The ESR methods detailed above are well-established for characterizing interactions between proteins and membranes and have previously been used to characterize the membrane-bound structural features of the wCpx1 CTD, as well as other proteins.[41,44] We investigated whether similar results could be obtained using fluorescence-based methods. Individual residues spanning the terminal 21 residues of the mCpx1 CTD were mutated to tryptophan and fluorescence spectra (see methods) were measured for these variants in the absence and presence of SUVs composed of 85% POPC/15% POPS. Spectra for SUV-bound mCpx1 CTD showed a clear shift in the wavelength of maximum fluorescence relative to the unbound mCpx1 CTD, with the shift being more pronounced for residues expected to partition into the membrane based on the ESR data (Figure 7 (A), S7(A)). Data between residues 113 and 124 showed oscillations with a 3–4 residue periodicity, which could be reasonably fit with either a fixed periodicity of 3.6 (black: $R^2 = 0.67$) or allowing the periodicity to float (red, periodicity = 3.98, $R^2 = 0.69$, Figure 7(B), S7(B))). Data in the CT-motif region (residues 128–134) exhibited only a weak periodicity, modulating a nearly monotonic decrease in wavelength shift. This method relies on the stability of the structure being assessed being sufficient to prevent perturbations due to the introduction of the probe itself. In this case, it may be that the shorter CT-motif is not sufficiently stable or cooperative to prevent perturbation by the introduction of Trp residues. Nevertheless, fits to the weak periodicity of these data are consistent with a helical structure (Figure 7(C), S7(C)). Data for residues 125–128, including the PGP sequence separating the AH- and CT-motifs, exhibited higher frequency oscillations, inconsistent with helical structure, consistent with evidence above from NMR and ESR suggesting that this region forms a break or kink between the AH- and CT-motifs. Fits to the entire region (residues 113–134) to a fixed or floating periodicity gave lower R^2 values (Figure 7(D), S7(D)). Overall, these data suggests that

the Trp-fluorescence agree well with the ESR data and accurately report on the membrane interactions of the mCpx1 AH-motif, but are less clear, compared with the ESR data, in reporting on CT-motif structure.

Interactions between the mCpx1 CTD and LUVs depend strongly on lipid composition

It has previously been established that the mCpx1 CTD senses curvature and preferentially interacts with SUVs rather than large unilamellar vesicles (LUVs).[34,35,38,66] It has also been shown that the wCpx1 CTD interacts preferentially with LUVs composed of lipids with increased acyl chain disorder and that such lipids induce helical structure, as observed in the presence of SUVs.[34] We investigated whether the mCpx1 CTD shows similar preferential binding to LUVs based on lipid composition. NMR 2D {^{15}N-^{1}H} HSQC spectra of the mCpx1 CTD in the presence of LUVs composed of 85% POPC/15% POPS showed only minor differences (Figure 8(A)), with small decreases in the intensities of peaks from the AH- and CT-motif regions of LUV-bound spectra relative to the free protein (Figure 8 (B)), consistent with previously reported preliminary data obtained using full-length mCpx1.[34] While CD spectra in the presence of LUVs were extremely noisy due to scattering, there was no evident change in secondary structure in the presence of LUVs relative to the free protein (Figure S8).

In contrast, NMR HSQC spectra of the mCpx1 CTD in the presence of LUVs composed of 60% DOPC/25% DOPE/15% DOPS showed marked differences relative to the free protein (Figure 8 (A)). There was both a global decrease in the intensities of peaks in the LUV-bound spectra and more pronounced decreases in the intensities of peaks in both the N- and C-termini (Figure 8(C)). The intensities decreased further with higher lipid concentrations relative to protein concentrations. This global decrease is explained at least in part by precipitation of some fraction of the LUV-bound complex in all samples, an effect which was only ever observed under these conditions and was reproducible for multiple LUV preparations and protein samples. The spectra of LUV-bound samples were stable over stretches of a few days, however, suggesting that a stable equilibrium is formed within the samples after an initial precipitation event. The global intensity changes were observable at lower lipid concentrations, before effects specific to the C-terminal end appear, and increased as lipid concentrations increased relative to protein concentrations (Figure S9).

These data suggest that two processes occur in with the mCpx1 CTD in the presence of these LUVs. At lower lipid concentrations, there is a global interaction event that induces aggregation or precipitation of a fraction of the protein and lipid in the samples, possibly through multivalent interactions between the entire sequence of mCpx1 CTD and the LUVs or through crowding of multiple proteins onto the vesicle surface (Figure S9(A)). At higher lipid concentrations, the protein that remains in solution interacts with the LUVs via specific motifs along the protein. The first 10–15 residues of the mCpx1 CTD, which encompasses the AH2-motif region, and the terminal 35 residues, which encompass the AH- and CT-motifs, all show more pronounced intensity changes in the presence of LUVs (Figure S9(B)). These data suggest that the interactions between the mCpx1 CTD and LUVs depends strongly on lipid composition and encompass more complex processes that require further study.

Discussion

Delineating the mechanisms by which complexins regulate SV exocytosis has remained a significant challenge since these proteins were discovered and is complicated by the evolutionary divergences of complexin function in preventing spontaneous SV release.[15] While previous work has been able to pinpoint the complexin CTD as critical to these differences,[36,38–40,45] their mechanistic and structural bases remain mysterious. We characterized the structural and dynamical features of the mCpx1 CTD in the absence and presence of lipid micelles and vesicles to begin to reconcile the differences between vertebrate and invertebrate complexin function. Though largely unstructured in the absence of lipids, the CTD forms two helical motifs spanning residues 115–124 (AH-motif) and 128–133 (CT-motif) in the presence of either micelles or SUVs. These two helices are connected by a PGP sequence that likely deviates from helical structure and is somewhat flexible, as indicated by secondary structure analysis in the micelle bound state, by fluorescence measurements showing non-helical periodicity for the PGP linker and by DEER measurements suggesting that the orientation of the helices with respect to each other differs between the micelle-bound and SUV-bound forms of the CTD. Vesicle binding and formation of these structural features in the C-terminus of the CTD is insensitive to changes in lipid saturation (DO or PO lipids) or PC vs. PE content (50:35 or 85:0) for SUVs. In contrast, interactions between the mCpx1 CTD and LUVs depends dramatically on lipid saturation levels, with only weak binding observed for LUVs composed PO lipids. For LUVs composed of DO lipids, stronger binding is observed in both the C- and N-terminal regions of the CTD, but this is accompanied by a process that results in precipitation of a fraction of the sample. Notably, we previously observed that the AH-motif of wCpx1 bound only weakly and without helix formation to LUVs composed of PO lipids, but bound more strongly and formed helical structure in the presence of DO lipid LUVs. We interpreted this to reflect an increase in lipid packing defects associated with the greater fraction of unsaturated acyl chains in the DO lipid LUVs. In contrast, in SUVs, the very high degree of curvature creates ample packing defects irrespective of acyl chain saturation, thus binding is observed for either PO or DO lipid SUVs.

A recent report[37] noted the amphipathic nature of the C-terminal 21 residues of mouse complexin 2, which are 95% identical to C-terminal 21 residues of mCpx1, and proposed that this region forms a helix in the presence of membranes that is kinked by the PGP sequence. This study suggested that this region could insert into the bilayer as a trans-membrane helix, assemble into multimeric pores and remodel membrane curvature, and that a similar process could contribute to regulation of fusion pore dynamics during SV release. Our cwESR and fluorescence experiments are not inconsistent with this model. Our pulsed ESR distance measurements, however, would be expected to exhibit both inter- and intra-molecular distances in the case of an oligomer pore structure, and we do not observe this. However, the pulsed ESR experiments were only performed using SUVs composed of DO lipids, whereas Courtney et al.[37] used LUVs or GUVs composed of DO lipids. Indeed, for CTD samples with LUVs containing DO lipids, we observed sample precipitation, which would be consistent with a membrane disruption/remodeling process. That we do not observe this for SUVs composed of either PO or DO lipids may result from the already very

high curvature of these vesicles, which appears to match the diameter of vesicles remodeled from larger structures.[37] The lipid composition and curvature dependence of such processes remain to be characterized in greater detail.

There are both similarities and differences in the membrane-bound structures of the mCpx1 CTD and the wCpx1 CTD (Figure 9(A)). In the absence of lipids, both CTDs are largely disordered outside of a helical AH2 region. The AH2-motif helix is significantly longer in the mCpx1 CTD and is separated from the helical AH-motif by 25 residues vs. only 6 residues in wCpx1. It should also be noted that though the chemical shifts in the AH2-motif region in the mCpx1 CTD are consistent with helical structure formation, the region does not show inter-residue NOEs or strong indications of structure in ps-ns relaxation measurements, suggesting that the region might be forming a transient or highly flexible helix. At present, the role the AH2-motif in complexin function is unclear.

Both the mCpx1 wCpx1 CTDs feature a helical AH-motif when bound to micelles or SUVs, but this helical structure is considerably shorter in the mCpx1 CTD (~10 residues) than in wCpx1 (~27 residues).[41] Helix formation by the wCpx1 AH-motif requires membrane bilayers with high curvature or unsaturated acyl chains; mCpx1 binds only very weakly to LUVs composed of PO lipids even at very high lipid concentrations (Figure 8(B)), with CD data indicating no secondary structure formation (Figure S8), suggesting that helix formation in the mCpx1 AH-motif may also depend on membrane curvature, likely because of associated membrane packing defects.

We previously reported that the CT-motif of the mCpx1 CTD likely forms helical structure in its micelle-bound state based on chemical shifts and computational modelling.[34,38] Here we substantiated this observation using measurements of NOEs and backbone dynamics, and, most importantly, extended it to the SUV-bound protein using ESR and fluorescence experiments. The mCpx1 CT-motif differs from that of wCpx1, which remains unstructured when bound to membranes. Notably, the mCpx1 CT-motif is unable to substitute for the wCpx1 CT-motif in living worms.[38] an observation that was somewhat puzzling in the absence of more complete structural information for the mCpx1 CTD.

In light of the new results presented here, the structural differences between the CTDs of the mCpx1 and wCpx1 proteins suggest an intriguing possibility for the functional differences between the proteins. We previously showed that the mCpx1 AH-motif cannot replace the much longer wCpx1 AH-motif.[38] We also noted that the helical structure of the wCpx1 AH-motif exhibits a pi-bulge centered around G116,[34,41] and that this bend or kink in the longer AH-motif helix is functionally important.[41] Our results now indicate that the mCpx-1 AH- and CT-motifs together form a nearly continuous helical structure. We posit that that the PGP sequence separating the two helical motifs in the mCpx1 CTD may play a similar role to that of G116 in wCpx1 by generating a kinked helical structure. This is supported by our DEER measurements indicating that the SUV-bound CT-motif is not co-linear with the AH-motif in the SUV-bound state. In this case, residues 115–134 of mCpx1 may in fact constitute a single AH-motif analogous to that of wCpx-1, while the CT-motif of the worm protein may be entirely lacking in the mouse protein. This would explain both the failure of the mouse CT-motif to substitute for the worm CT-motif, as well as the failure of the

previously delineated mouse AH-motif, which we now propose is incomplete, to substitute for the worm AH-motif. Finally, we have shown that the worm CT-motif is critical for the inhibitory function of wCpx1. If mCpx1 is lacking an analogous CT-motif, this may explain the highly circumscribed inhibitory activity of the mouse protein.

Additional possibilities exist for how the structural features of the mCpx1 CTD underlie functional divergence from the wCpx1 CTD. While the CT-motif is critical for both CTD lipid binding and inhibitory function in wCpx1, disrupting the structural features of the AH-motif generates a similar phenotypes *in vivo*[36] but only disrupts CTD lipid binding within locally.[34] These data suggest that the AH-motif helix plays a role beyond contributing to lipid binding, such as interacting with a binding partner. The dissimilarities in the structural features of the mCpx1 AH-motif compared to that of wCpx1 may preclude such interactions when the mCpx1 AH-motif is substituted in living worms.

There is a single dominant worm complexin, while there are two dominant splice isoforms in flies and four isoforms in mammals,[6,18,25,46–48] all of which show wide sequence variation in their CTDs (Figure 9(B)). Complexin CTDs also feature known isoform-specific post-translational modifications (PTMs) with the potential to alter lipid or protein interactions, including farnesylation and phosphorylation.[39,46–51] Fly complexin represents a particularly intriguing target for future research in that its two dominant isoforms diverge only in their C-termini, with one isoform (7A) containing a farnesylation motif while the other isoform (7B) does not.[47–48] We previously analyzed the putative AH-motif of fly complexin 7B (fCpx7B) and showed that it likely resembles the AH-motif of wCpx1, being longer than that of mCpx1 and featuring a glycine residue that likely results in a kinked helix.[36,41] However, a potential fCpx7B CT-motif, demarcated by a proline residue following the putative AH-motif (Figure 9(B)), bears some resemblance to the mCpx1 CT-motif (PLRNLF vs. PLQDMFKK) and would form a highly amphipathic helix. Removal of fly complexin results in a massive increase in spontaneous neurotransmitter release at fly neuro-muscular junctions,[17,39,45] suggesting that fly complexin may more closely resemble the worm protein, but the contributions of the individual fly isoforms, 7A and 7B, to inhibition of release is complex.[47,49] Future studies of these differing isoforms and comparison with other prenylated and unprenylated variants may help further bridge the gaps in our understanding of the divergent functions of complexins.

Notably, phosphomimetic mutations of complexin at known phosphorylation sites modulate the recently reported ability of the mCpx2 CTD to form or stabilize pores in membranes.[37] Different complexin variants and modifications offer opportunities to explore the connections between CTD structure and membrane interactions and complexin function and how these connections vary between vertebrates and invertebrates. The detailed structural insights we have provided here for the mCpx1 CTD and comparison of these with similar insights obtained previously for the wCpx1 CTD have begun to shed light on potential structural bases for functional differences between these proteins.

Materials and Methods

Protein expression and purification:

Proteins were expressed and purified as described previously.[34] In brief, his_6-SUMO tagged constructs were expressed at 37 °C in BL21 (DE3) cells in either LB or isotopically-enriched minimal medium, induced with IPTG between O.D. ~ 0.6–0.8 and spun down after 3–4 hours. Cells were lysed by sonication and the cell lysate was centrifuged at 40,000 rpm for 30 min – 1 hour. The supernatant was then passed over a NiNTA column and the his_6-SUMO tag was cleaved with SUMO protease. A second run of the NiNTA column removed the his_6-SUMO tag. Proteins were then dialyzed into dH_2O through multiple rounds of dialysis, lyophilized, and stored at −20 °C. All isotopes were purchased from Cambridge Isotope Laboratories.

Liposome preparation:

All lipids were purchased from Avanti Polar Lipids and stored at −20 °C. Lipids were mixed and residual solvent removed under vacuum for 1–2 hours. To prepare SUVs, the lipid mixtures were resuspended in buffer, clarified via bath sonication, and ultracentrifuged at 60,000 rpm for 1 hour. To prepare LUVs, the lipid mixtures were resuspended in buffer, subjected to ten successive rounds of freeze–thaw in liquid nitrogen-warm water baths, and extruded 21 times through polycarbonate films with a pore size of 200 nm in a 1 mL Avanti Mini-Extruder (Avanti Polar Lipids). Lipid mixtures were stored at 4 °C and used within one week of lipid preparation. Lipid concentrations are based on the amount of lipid added in the initial mixture.

NMR assignments and data analysis:

NMR spectra were processed using NMRpipe,[52] analyzed using NMRFAM-sparky,[53] and NMRbox.[54] TALOS-N was used to generate secondary structure predictions.[55] ΔCα-ΔCβ calculations were performed by subtracting experimentally determined Cα and Cβ values for the mCpx1 CTD from random coil values calculated using Poulsen IDP/IUP random coil chemical shifts.[56–60] The unbound mouse complexin CTD was assigned using triple resonance data collected with 1.3 mM {^{15}N-^{13}C} mCpx1 CTD (residues 71–134) at 10 °C on a Bruker Avance III spectrometer at 700 MHz (^{1}H) (New York Structural Biology Center) using HNCACB (16 transients, 144 (^{13}C) × 64 (^{15}N) x1024 (^{1}H) complex points), CBCA(CO)NH (16 transients, 144 (^{13}C) × 64 (^{15}N) x1024 (^{1}H) complex points), HN(CA)CO (16 transients, 128 (^{13}C) 64 (^{15}N) x1024 (^{1}H) complex points), and HNCO (8 transients, 96 (^{13}C) × 64 (^{15}N) x1024 (^{1}H) complex points) spectra. The micelle-bound mouse complexin CTD was assigned using triple resonance data collected with 500 μM {^{15}N-^{13}C} mCpx1 CTD (residues 71–134) + 60 mM DPC at 40 °C with {^{15}N-^{13}C} labeled mCpx1 CTD on a Bruker Avance III spectrometer at 600 MHz (^{1}H) (Weill Cornell NMR core), using CBCA(CO)NH (16 transients, 128 (^{13}C) × 70 (^{15}N) x1024 (^{1}H) complex points), HNCA (16 transients, 96 (^{13}C) × 70 (^{15}N) x1024 (^{1}H) complex points), HNCACB (16 transients, 128 (^{13}C) × 70 (^{15}N) x1024 (^{1}H) complex points), HN(CA)CO (16 transients, 94 (^{13}C) × 74 (^{15}N) x1024 (^{1}H) complex points), HNCO (16 transients, 112 (^{13}C) × 70 (^{15}N) x1024 (^{1}H) complex points), and HN(CACO)NH (32 transients, 60 (^{15}N) × 60 (^{15}N) x1024 (^{1}H) complex points) spectra. HSQC-NOESY-HSQC and NOESY-HSQC spectra

were collected with 500 μM {^{15}N-^{2}H} mCpx1 CTD + 60 mM DPC at 40 °C (24 transients, 96 (^{15}N) x72 (^{15}N) x1024 (^{1}H) complex points, τ_{mix} = 150 ms) and 40 °C (16 transients, 256 (^{1}H) × 64 (^{15}N) × 1024 (^{1}H) complex points, τ_{mix} = 100 ms), respectively, on a Bruker Avance spectrometer at 800 MHz (^{1}H) (New York Structural Biology Center). Temperature series of both free and micelle-bound mCpx1 CTD facilitated the transfer of assignments in the lipid-binding region of the protein to spectra collected at different temperatures. CSPs were calculated using standard equations,[61] with α = 0.14:

$$\Delta\delta = \sqrt{\frac{1}{2}\left(\delta_H^2 + (\alpha * \delta)_N^2\right)}$$

Intensity ratios for SUV-bound mCpx1 CTD relative to unbound mCpx1 CTD were performed using 200 μM ^{15}N-labeled mCpx1 CTD (32 scans, 174 (^{15}N) x2048 (^{1}H) complex points), 200 μM ^{15}N-labeled mCpx1 CTD + 10 mM 60% DOPC/25% DOPE/15% DOPS (32 scans, 174 (^{15}N) x2048 (^{1}H) complex points), 200 μM ^{15}N-labeled mCpx1 CTD + 10 mM 85% POPC/15% POPS (32 scans, 174 (^{15}N) x2048 (^{1}H) complex points) collected at 10 °C with on a Bruker Avance III spectrometer at 600 MHz (^{1}H) (Weill Cornell NMR core). Intensity ratios for LUV-bound mCpx1 CTD relative to unbound mCpx1 CTD were performed using 200 μM ^{15}N-labeled mCpx1 CTD (32 scans, 174 (^{15}N) x2048 (^{1}H) complex points), 200 μM ^{15}N-labeled mCpx1 CTD + 20 mM 60% DOPC/25% DOPE/15% DOPS (32 scans, 174 (^{15}N) x2048 (^{1}H) complex points), 200 μM ^{15}N- labeled mCpx1 CTD + 0.5 mM, 1 mM, 5 mM or 20 mM 85% POPC/15% POPS (32 scans, 174 (^{15}N) x2048 (^{1}H) complex points), 50 μM ^{15}N-labeled mCpx1 CTD (256 scans, 174 (^{15}N) x2048 (^{1}H) complex points), and 50 μM ^{15}N-labeled mCpx1 CTD + 15 mM 85% POPC/15% POPS (256 scans, 174 (^{15}N) x2048 (^{1}H) complex points) collected at 10 °C with on a Bruker Avance III spectrometer at 600 MHz (^{1}H) (Weill Cornell NMR core).

NMR relaxation experiments:

NMR ps-ns relaxation experiments were collected with 200 μM ^{15}N-labeled mCpx1 CTD with and without 71 mM DPC micelles (Avanti) in 20 mM phosphate, pH 6.1, 100 mM NaCl, 1 mM TCEP, 5% D_2O. Experiments were collected at 10 °C (free) and 40 °C (micelle-bound) on a Bruker Avance Spectrometer at 800 MHz (^{1}H) and on a Bruker Avance Spectrometer at 900 MHz (^{1}H) (New York Structural Biology Center). Data were analyzed using NMRFAM-sparky[53] and the sparky2rate script in NMRbox[54] to analyze the data in CurveFit.[62]

R_1 measurements were collected at 800 MHz (^{1}H) using delays of {0.001, 0.08, 0.2, 0.4, 0.6, 0.8, 0.9, 0.2}s with recycling delays of 1.5 s, 32 scans and 148 (^{15}N) × 1024 (^{1}H) complex points for the free protein and {0.001, 0.08, 0.1, 0.2, 0.4, 0.6, 0.7, 0.1}s with recycling delays of 1.6 s, 32 scans and 200 (^{15}N) × 1024 (^{1}H) complex points for the micelle-bound protein. R_1 measurements were collected at 900 MHz (^{1}H) using delays of {0.001, 0.08, 0.1, 0.2, 0.4, 0.6, 0.8, 0.2}s with recycling delays of 2.5 s, 16 scans and 240 (^{15}N) × 1024 (^{1}H) complex points (900 MHz) for the free and micelle-bound proteins. R_2 measurements were collected at 800 MHz (^{1}H) using delays of {0, 0.016, 0.032, 0.064, 0.096, 0.112, 0.128, 0.032}s with recycling delays of 2 s, 32 scans and 200 (^{15}N) × 1024 (^{1}H) complex points

for the free protein and {0, 0.016, 0.032, 0.064, 0.080, 0.096, 0.112, 0.032}s with recycling delays of 2 s, 32 scans and 200 (^{15}N) × 1024 (^{1}H) complex points for the micelle-bound protein. R_2 measurements were collected at 900 MHz (^{1}H) using delays {0, 0.016, 0.032, 0.064, 0.08, 0.096, 0.112, 0.032}s with recycling delays of 2.5 s, 24 scans (free) or 32 scans (micelle-bound) and 240 (^{15}N) × 1024 (^{1}H) complex points (900 MHz). {^{15}N-^{1}H} heteronuclear NOE experiments were collected at 800 MHz (^{1}H) in triplicate with saturation periods of 4 s with an additional 2 s recycling delay for a total interscan delay of 6 s and control experiments were collected with a total interscan delay of 7 s with 48 scans and 192 (^{15}N) × 1024 (^{1}H) complex points for both free and micelle-bound proteins.

SUV-bound R_2 measurements were collected at 800 MHz (^{1}H) with 190–200 μM ^{15}N-labeled mCpx1 CTD and 2.8 mM SUV composed of 60% DOPC/25% DOPE/15% DOPS or 3 mM SUV composed of 85% POPC/15% POPS in in 20 mM phosphate, pH 6.1, 100 mM NaCl, 1 mM TCEP, 0.1 mM EDTA, 5% D_2O. Experiments were collected using delays of {0.016, 0.032, 0.064, 0.080, 0.096, 0.112, 0.032}s with recycling delays of 2.4 s, 32 scans and 214 (^{15}N) × 1024 (^{1}H) complex points. Relaxation rates for the SUV-bound protein were subtracted from the free protein to evaluate the change in R_2s upon SUV binding.

CD spectroscopy:

CD spectra were collected at 25 °C using an AVIV Biomedical Model 410CD Spectrometer with one nm wavelength steps from 300 nm to 190 nm, 1 scan with a 5 second averaging time, and a two minute temperature equilibration. The CD buffer was 20 mM sodium phosphate, pH 6.1, 100 mM NaCl. Protein concentrations were calculated using A280 values, with an extinction coefficient of 1,490 M^{-1} cm^{-1} based on the CTD amino acid sequence, and all spectra were collected with an estimated protein concentration of 80–200 μM.

Fluorescence Experiments:

Tryptophan fluorescence emission spectra were collected as described previously.[63] Tryptophan fluorescence was excited at 295 nm and emission spectra were collected from 300–500 nm on a SpectraMax M5 plate reader (Molecular Devices). Each well contained 20 μM mCpx1 CTD and 1 mM 85% POPC/15% POPS in 50 mM Tris-Cl, pH 8.0, 150 mM NaCl, 5 mM EDTA. The wavelength of maximum fluorescence was determined by fitting individual tryptophan fluorescence spectra from four data sets as described in.[64] The shift in maximum fluorescence was calculated by subtracting the maximum fluorescence for lipid-bound mCpx1 CTD from the maximum fluorescence of unbound mCpx1 CTD for individual datasets. The change in the wavelength of maximum fluorescence was fit to the following equation.

$$\Delta Wavelength of Max Fluorescence = A * \sin\left(2 * \pi * \frac{N}{periodicity} + B\right) + C$$

where N is the residue number, A is a scaling factor, B is a phasing correction, C is an offset and periodicity is the periodicity of the sin wave. The periodicity was either fixed to 3.6 or globally fit for all the data sets. B was globally fit among all the data sets, while A and

C were set as local parameters for fits of each data set. Data were fit using Mathematica software (Wolfram).

Power saturation ESR:

The CW-ESR spectra were collected on an ELEXSYS ESR spectrometer (Bruker Instruments, Billerica, MA) at X-band (9.5 GHz) at RT. The proteins were spin labeled using MTSL (S-(2,2,5,5-tetramethyl-2, 5-dihydro-1H-pyrrol-3-yl) methyl methanesulfonothioate) as previously described.[34] The power saturation continuous wave ESR measurements were performed as reported previously.[41] All experiments were done at least in duplicate or triplicate to ensure reproducibility. Phi parameters were fit using the following equation.

$$\varphi = A * \sin\left(2 * \pi * \frac{N}{periodicity} + B\right) + C$$

where N is the residue number, A is a scaling factor, B is a phasing correction, C is an offset and periodicity is the periodicity of the sin wave. A, B and C were floated during the fit, while the periodicity was either fixed to 3.6 or floated during the fit. Data were fit using Mathematica software (Wolfram).

Double electron–electron resonance (DEER) spectroscopy.

Approximately 50 μM double spin-labeled proteins were incubated with 10 mM SUVs (60% DOPC/25% DOPE/15% DOPS) or DPC micelles for 10 minutes at 25 °C. Deuterated glycine was added to reach a final concentration of 20% (w/v). The samples were transferred to an ESR tube and rapidly frozen in liquid nitrogen. Standard four-pulse DEER ESR experiments were performed using a Bruker 34 GHz Q-band ELEXSYS ESR spectrometer (Bruker Instruments, Billerica, MA) at 60 K. A pulse sequence with π/2-π - π pulse widths of 16 ns, 32 ns and 32 ns, respectively and a 32 ns π pump pulse was routinely used or adjusted by the standard setup experiments. Typical evolution times were 6 μs with signal averaging from 8–10 hours. The distances were reconstructed from the baseline-subtracted signals using the singular value decomposition (SVD) method.[65] The distance distribution is further fitted by a Gaussian distribution to obtain the position and width of the peak. The data were analyzed using Origin (OriginLab Inc.). All DEER experiments were done at least in triplicate to ensure reproducibility.

Supplementary Material

Refer to Web version on PubMed Central for supplementary material.

Acknowledgements

We would like to thank Dr. Shibani Bhattacharya (NYSBC) and Dr. Clay Bracken (WCMC) for their continued assistance in the use of NMR spectrometers and implementing experimental methods. D.E. would like to acknowledge support by NIH grants R35GM136686 and R01GM117518 and data collection as a member of the New York Structural Biology Center. The data collected at NYSBC were made possible by a grant from ORIP/NIH facility improvement grant CO6RR015495. The 700 MHz spectrometer was purchased with funds from NIH grant S10OD018509. Data collected using the 800 MHz Avance III spectrometer is supported by NIH grant S10OD016432. The 900 MHz NMR spectrometers were purchased with funds from NIH grant P41GM066354 and the New York State Assembly. Some of the work presented here was conducted at the Center on Macromolecular Dynamics by NMR Spectroscopy located at the New York Structural Biology Center, supported by a grant

from the NIH National Institute of General Medical Sciences (GM118302). J.H.F was supported by NIH grants R01GM123779 and P41GM103521. The Q-band Bruker ESR spectrometer for DEER is supported by NIH grant 1S10OD021543.

DATA AVAILABILITY

Data will be made available on request.

Abbreviations used:

SVs	synaptic vesicles
NTD	N-terminal domain
AHD	accessory helical domain
CHD	central helix domain
CTD	C-terminal domain
ID	intrinsically disordered
wCpx1	worm (*Caenorhabditis elegans*) complexin 1
AH	amphipathic helix
CT	C-terminal motif
mCpx1	mouse (*Mus musculus*) complexin 1
SUV	small unilamellar vesicle
LUV	large unilamellar vesicle
NMR	nuclear magnetic resonance
CD	circular dichroism
ESR	electron spin resonance
cwESR	continuous wave ESR
DEER	double electron–electron resonance
DPC	dodecylphosphocholine
POPC	1-palmitoyl-2-oleoyl-glycero-3-phosphocholine
POPS	1-palmitoyl-2-oleoyl-sn-glycero-3-phospho-L-serine
DOPC	1,2-dioleoyl-sn-gly cero-3-phosphocholine
DOPE	1,2-dioleoyl-sn-glycero-3-phosphoe thanolamine
DOPS	1,2-dioleoyl-sn-glycero-3-phospho-L-serine
DO	1,2-dioleoyl

PO	1-palmitoyl-2-oleoyl

References

1. Südhof TC, (2012). The presynaptic active zone. Neuron 75, 11–25. 10.1016/j.neuron.2012.06.012. [PubMed: 22794257]
2. Rizo J, Rosenmund C, (2008). Synaptic vesicle fusion. Nat. Struct. Mol. Biol 15, 665–674. 10.1038/nsmb.1450. [PubMed: 18618940]
3. Südhof TC, (2013). Neurotransmitter release: The last millisecond in the life of a synaptic vesicle. Neuron 80, 675–690. 10.1016/j.neuron.2013.10.022. [PubMed: 24183019]
4. Südhof TC, Rizo J, (2011). Synaptic vesicle exocytosis. Cold Spring Harb. Perspect. Biol 3 10.1101/cshperspect.a005637.
5. Rizo J, Xu J, (2015). The Synaptic Vesicle Release Machinery. Annu. Rev. Biophys 44, 339–367. 10.1146/annurev-biophys-060414-034057. [PubMed: 26098518]
6. McMahon HT, Missler M, Li C, Südhof TC, (1995). Complexins: Cytosolic proteins that regulate SNAP receptor function. Cell 83, 111–119. 10.1016/0092-8674(95)90239-2. [PubMed: 7553862]
7. Ishizuka T, Saisu H, Odani S, Abe T, (1995). Synaphin: A protein associated with the docking/fusion complex in presynaptic terminals. Biochem. Biophys. Res. Commun 213, 1107–1114. 10.1006/bbrc.1995.2241. [PubMed: 7654227]
8. Ishizuka T, Saisu H, Suzuki T, Kirino Y, Abe T, (1997). Molecular cloning of synaphins/complexins, cytosolic proteins involved in transmitter release, in the electric organ of an electric ray (Narke japonica). Neurosci. Lett 232, 107–110. 10.1016/S0304-3940(97)00586-7. [PubMed: 9302098]
9. Schneggenburger R, Rosenmund C, (2015). Molecular mechanisms governing Ca2+ regulation of evoked and spontaneous release. Nat. Neurosci 18, 935–941. 10.1038/nn.4044. [PubMed: 26108721]
10. Reim K, Mansour M, Varoqueaux F, McMahon HT, Südhof TC, Brose N, Rosenmund C, (2001). Complexins regulate a late step in Ca2+-dependent neurotransmitter release. Cell 104, 71–81. 10.1016/S0092-8674(01)00192-1. [PubMed: 11163241]
11. Glynn D, Drew CJ, Reim K, Brose N, Morton AJ, (2005). Profound ataxia in complexin I knockout mice masks a complex phenotype that includes exploratory and habituation deficits. Hum. Mol. Genet 14, 2369–2385. 10.1093/hmg/ddi239. [PubMed: 16000319]
12. Xu Y, Zhao XM, Liu J, Wang YY, Xiong LL, He XY, Wang TH, (2020). Complexin I knockout rats exhibit a complex neurobehavioral phenotype including profound ataxia and marked deficits in lifespan, Pflugers Arch. Eur. J. Physiol 472, 117–133. 10.1007/s00424-019-02337-5. [PubMed: 31875236]
13. Redler S, Strom TM, Wieland T, Cremer K, Engels H, Distelmaier F, Schaper J, Küchler A, Lemke JR, Jeschke S, Schreyer N, Sticht H, Koch M, Lüdecke HJ, Wieczorek D, (2017). Variants in CPLX1 in two families with autosomal-recessive severe infantile myoclonic epilepsy and ID. Eur. J. Hum. Genet 25, 889–893. 10.1038/ejhg.2017.52. [PubMed: 28422131]
14. Karaca E, Harel T, Pehlivan D, Jhangiani SN, Gambin T, Coban Akdemir Z, Gonzaga-Jauregui C, Erdin S, Bayram Y, Campbell IM, Hunter JV, Atik MM, Van Esch H, Yuan B, Wiszniewski W, Isikay S, Yesil G, Yuregir OO, Tug Bozdogan S, Aslan H, Aydin H, Tos T, Aksoy A, De Vivo DC, Jain P, Geckinli BB, Sezer O, Gul D, Durmaz B, Cogulu O, Ozkinay F, Topcu V, Candan S, Cebi AH, Ikbal M, Yilmaz Gulec E, Gezdirici A, Koparir E, Ekici F, Coskun S, Cicek S, Karaer K, Koparir A, Duz MB, Kirat E, Fenercioglu E, Ulucan H, Seven M, Guran T, Elcioglu N, Yildirim MS, Aktas D, Alikaşifoğlu M, Ture M, Yakut T, Overton JD, Yuksel A, Ozen M, Muzny DM, Adams DR, Boerwinkle E, Chung WK, Gibbs RA, Lupski JR, (2015). Genes that Affect Brain Structure and Function Identified by Rare Variant Analyses of Mendelian Neurologic Disease. Neuron 88, 499–513. 10.1016/j.neuron.2015.09.048. [PubMed: 26539891]
15. Trimbuch T, Rosenmund C, (2016). Should I stop or should I go? The role of complexin in neurotransmitter release. Nat. Rev. Neurosci 17, 118–125. 10.1038/nrn.2015.16. [PubMed: 26806630]
16. Brose N, (2008). For Better or for Worse: Complexins Regulate SNARE Function and Vesicle Fusion. Traffic 9, 1403–1413. 10.1111/j.1600-0854.2008.00758.x. [PubMed: 18445121]

17. Huntwork S, Littleton JT, (2007). A complexin fusion clamp regulates spontaneous neurotransmitter release and synaptic growth. Nat. Neurosci 10, 1235–1237. 10.1038/nn1980. [PubMed: 17873870]

18. Hobson RJ, Liu Q, Watanabe S, Jorgensen EM, (2011). Complexin maintains vesicles in the primed state in C. elegans. Curr. Biol 21, 106–113. 10.1016/j.cub.2010.12.015. [PubMed: 21215631]

19. Martin JA, Hu Z, Fenz KM, Fernandez J, Dittman JS, (2011). Complexin has opposite effects on two modes of synaptic vesicle fusion. Curr. Biol 21, 97–105. 10.1016/j.cub.2010.12.014. [PubMed: 21215634]

20. Xue M, Reim K, Chen X, Chao HT, Deng H, Rizo J, Brose N, Rosenmund C, (2007). Distinct domains of complexin I differentially regulate neurotransmitter release. Nat. Struct. Mol. Biol 14, 949–958. 10.1038/nsmb1292. [PubMed: 17828276]

21. Maximov A, Tang J, Yang X, Pang ZP, Südhof TC, (2009). Complexin controls the force transfer from SNARE complexes to membranes in fusion. Science (80-) 323, 516–521. 10.1126/science.1166505.

22. Yang X, Cao P, Südhof TC, (2013). Deconstructing complexin function in activating and clamping Ca 2+-triggered exocytosis by comparing knockout and knockdown phenotypes. Proc. Natl. Acad. Sci. U. S. A 110, 20777–20782. 10.1073/pnas.1321367110. [PubMed: 24297916]

23. Lai Y, Choi UB, Zhang Y, Zhao M, Pfuetzner RA, Wang AL, Diao J, Brunger AT, (2016). N-terminal domain of complexin independently activates calcium-triggered fusion. Proc. Natl. Acad. Sci. U. S. A 113, E4698–E4707. 10.1073/pnas.1604348113. [PubMed: 27444020]

24. Radoff DT, Dong Y, Snead D, Bai J, Eliezer D, Dittman JS, (2014). The accessory helix of complexin functions by stabilizing central helix secondary structure. Elife 3, 1–17. 10.7554/eLife.04553.

25. Pabst S, Hazzard JW, Antonin W, Südhof TC, Jahn R, Rizo J, Fasshauer D, (2000). Selective interaction of complexin with the neuronal SNARE complex determination of the binding regions. J. Biol. Chem 275, 19808–19818. 10.1074/jbc.M002571200. [PubMed: 10777504]

26. Chen X, Tomchick DR, Kovrigin E, Araç D, Machius M, Südhof TC, Rizo J, (2002). Three-dimensional structure of the complexin/SNARE complex. Neuron 33, 397–409. 10.1016/S0896-6273(02)00583-4. [PubMed: 11832227]

27. Bracher A, Kadlec J, Betz H, Weissenhorn W, (2002). X-ray structure of a neuronal complexin-SNARE complex from squid. J. Biol. Chem 277, 26517–26523. 10.1074/jbc.M203460200. [PubMed: 12004067]

28. Choi UB, Zhao M, Zhang Y, Lai Y, Brunger AT, (2016). Complexin induces a conformational change at the membrane-proximal C-terminal end of the SNARE complex. Elife 5 10.7554/eLife.16886.

29. Bera M, Ramakrishnan S, Coleman J, Krishnakumar SS, Rothman JE, (2022). Molecular determinants of complexin clamping and activation function. Elife 11 10.7554/ELIFE.71938.

30. Brady J, Vasin A, Bykhovskaia M, (2021). The Accessory Helix of Complexin Stabilizes a Partially Unzippered State of the SNARE Complex and Mediates the Complexin Clamping Function *in Vivo* ENEURO.0526–20.2021 Eneuro 10.1523/ENEURO.0526-20.2021.

31. Vasin A, Volfson D, Littleton JT, Bykhovskaia M, (2016). Interaction of the Complexin Accessory Helix with Synaptobrevin Regulates Spontaneous Fusion. Biophys. J 111, 1954. 10.1016/J.BPJ.2016.09.017. [PubMed: 27806277]

32. Kümmel D, Krishnakumar SS, Radoff DT, Li F, Giraudo CG, Pincet F, Rothman JE, Reinisch KM, (2011). Complexin cross-links prefusion SNAREs into a zigzag array. Nat. Struct. Mol. Biol 188 (18), 927–933. 10.1038/nsmb.2101.

33. Trimbuch T, Xu J, Flaherty D, Tomchick DR, Rizo J, Rosenmund C, (2014). Re-examining how complexin inhibits neurotransmitter release: SNARE complex insertion or electrostatic hindrance? Elife 2014 10.7554/ELIFE.02391.

34. Snead D, Wragg RT, Dittman JS, Eliezer D, (2014). Membrane curvature sensing by the C-terminal domain of complexin. Nat. Commun 5, 4955. 10.1038/ncomms5955. [PubMed: 25229806]

35. Gong J, Lai Y, Li X, Wang M, Leitz J, Hu Y, Zhang Y, Choi UB, Cipriano D, Pfuetzner RA, Südhof TC, Yang X, Brunger AT, Diao J, (2016). C-terminal domain of mammalian complexin-1 localizes to highly curved membranes. Proc. Natl. Acad. Sci. U. S. A 113, E7590–E7599. 10.1073/pnas.1609917113. [PubMed: 27821736]
36. Wragg RT, Snead D, Dong Y, Ramlall TF, Menon I, Bai J, Eliezer D, Dittman JS, (2013). Synaptic Vesicles Position Complexin to Block Spontaneous Fusion. Neuron 77, 323–334. 10.1016/j.neuron.2012.11.005. [PubMed: 23352168]
37. Courtney KC, Wu L, Mandal T, Swift M, Zhang Z, Alaghemandi M, Wu Z, Bradberry MM, Deo C, Lavis LD, Volkmann N, Hanein D, Cui Q, Bao H, Chapman ER, (2022). The complexin C-terminal amphipathic helix stabilizes the fusion pore open state by sculpting membranes. Nat. Struct. Mol. Biol 2022, 1–11. 10.1038/s41594-021-00716-0.
38. Wragg RT, Parisotto DA, Li Z, Terakawa MS, Snead D, Basu I, Weinstein H, Eliezer D, Dittman JS, (2017). Evolutionary divergence of the c-terminal domain of complexin accounts for functional disparities between vertebrate and invertebrate complexins. Front. Mol. Neurosci 10 10.3389/fnmol.2017.00146.
39. Xue M, Lin YQ, Pan H, Reim K, Deng H, Bellen HJ, Rosenmund C, (2009). Tilting the Balance between Facilitatory and Inhibitory Functions of Mammalian and Drosophila Complexins Orchestrates Synaptic Vesicle Exocytosis. Neuron 64, 367–380. 10.1016/j.neuron.2009.09.043. [PubMed: 19914185]
40. Kaeser-Woo YJ, Yang X, Südhof TC, (2012). C-terminal complexin sequence is selectively required for clamping and priming but not for Ca 2+ triggering of synaptic exocytosis. J. Neurosci 32, 2877–2885. 10.1523/JNEUROSCI.3360-11.2012. [PubMed: 22357870]
41. Snead D, Lai AL, Wragg RT, Parisotto DA, Ramlall TF, Dittman JS, Freed JH, Eliezer D, (2017). Unique structural features of membrane-bound C-terminal domain motifs modulate complexin inhibitory function. Front. Mol. Neurosci 10 10.3389/fnmol.2017.00154.
42. Seiler F, Malsam J, Krause JM, Söllner TH, (2009). A role of complexin-lipid interactions in membrane fusion. FEBS Lett 583, 2343–2348. 10.1016/j.febslet.2009.06.025. [PubMed: 19540234]
43. Bodner CR, Dobson CM, Bax A, (2009). Multiple tight phospholipid-binding modes of α-synuclein revealed by solution NMR spectroscopy. J. Mol. Biol 390, 775. 10.1016/J.JMB.2009.05.066. [PubMed: 19481095]
44. Claxton DP, Kazmier K, Mishra S, McHaourab HS, (2015). Navigating Membrane Protein Structure, Dynamics, and Energy Landscapes Using Spin Labeling and EPR Spectroscopy. In: Methods Enzymol. Academic Press Inc., pp. 349–387. 10.1016/bs.mie.2015.07.026.
45. Cho RW, Song Y, Littleton JT, (2010). Comparative analysis of Drosophila and mammalian complexins as fusion clamps and facilitators of neurotransmitter release. Mol. Cell. Neurosci 45, 389–397. 10.1016/j.mcn.2010.07.012. [PubMed: 20678575]
46. Reim K, Wegmeyer H, Brandstätter JH, Xue M, Rosenmund C, Dresbach T, Hofmann K, Brose N, (2005). Structurally and functionally unique complexins at retinal ribbon synapses. J. Cell Biol 169, 669–680. 10.1083/jcb.200502115. [PubMed: 15911881]
47. Buhl LK, Jorquera RA, Akbergenova Y, Huntwork-Rodriguez S, Volfson D, Littleton JT, (2013). Differential regulation of evoked and spontaneous neurotransmitter release by C-terminal modifications of complexin. Mol. Cell. Neurosci 52, 161–172. 10.1016/j.mcn.2012.11.009. [PubMed: 23159779]
48. Iyer J, Wahlmark CJ, Kuser-Ahnert GA, Kawasaki F, (2013). Molecular mechanisms of COMPLEXIN fusion clamp function in synaptic exocytosis revealed in a new Drosophila mutant. Mol. Cell. Neurosci 56, 244–254. 10.1016/j.mcn.2013.06.002. [PubMed: 23769723]
49. Cho RW, Buhl LK, Volfson D, Tran A, Li F, Akbergenova Y, Littleton JT, (2015). Phosphorylation of Complexin by PKA Regulates Activity-Dependent Spontaneous Neurotransmitter Release and Structural Synaptic Plasticity. Neuron 88, 749–761. 10.1016/j.neuron.2015.10.011. [PubMed: 26590346]
50. Shata A, Saisu H, Odani S, Abe T, (2007). Phosphorylated synaphin/complexin found in the brain exhibits enhanced SNARE complex binding. Biochem. Biophys. Res. Commun 354, 808–813. 10.1016/j.bbrc.2007.01.064. [PubMed: 17266930]

51. Robinson SW, Bourgognon JM, Spiers JG, Breda C, Campesan S, Butcher A, Mallucci GR, Dinsdale D, Morone N, Mistry R, Smith TM, Guerra-Martin M, Challiss RAJ, Giorgini F, Steinert JR, (2018). Nitric oxide-mediated posttranslational modifications control neurotransmitter release by modulating complexin farnesylation and enhancing its clamping ability. PLoS Biol 16 10.1371/journal.pbio.2003611.
52. Delaglio F, Grzesiek S, Vuister G, Zhu G, Pfeifer J, Bax A, (1995). NMRPipe: A multidimensional spectral processing system based on UNIX pipes. J. Biomol. NMR 6, 277–293. 10.1007/BF00197809. [PubMed: 8520220]
53. Lee W, Tonelli M, Markley JL, (2015). NMRFAMSPARKY: enhanced software for biomolecular NMR spectroscopy. Bioinformatics 31, 1325–1327. 10.1093/bioinformatics/btu830. [PubMed: 25505092]
54. Maciejewski MW, Schuyler AD, Gryk MR, Moraru II, Romero PR, Ulrich EL, Eghbalnia HR, Livny M, Delaglio F, Hoch JC, (2017). NMRbox: A resource for biomolecular NMR computation. Biophys. J 112, 1529–1534. 10.1016/J.BPJ.2017.03.011. [PubMed: 28445744]
55. Shen Y, Bax A, (2013). Protein backbone and sidechain torsion angles predicted from NMR chemical shifts using artificial neural networks. J. Biomol. NMR 56, 227–241. 10.1007/s10858-013-9741-y. [PubMed: 23728592]
56. Kjaergaard M, Poulsen FM, (2011). Sequence correction of random coil chemical shifts: Correlation between neighbor correction factors and changes in the Ramachandran distribution. J. Biomol. NMR 50, 157–165. 10.1007/s10858-011-9508-2. [PubMed: 21604143]
57. Kjaergaard M, Brander S, Poulsen FM, (2011). Random coil chemical shift for intrinsically disordered proteins: Effects of temperature and pH. J. Biomol. NMR 49, 139–149. 10.1007/s10858-011-9472-x. [PubMed: 21234644]
58. Schwarzinger S, Kroon GJA, Foss TR, Chung J, Wright PE, Dyson HJ, (2001). Sequence-dependent correction of random coil NMR chemical shifts. J. Am. Chem. Soc 123, 2970–2978. 10.1021/ja003760i. [PubMed: 11457007]
59. Maltsev AS, Ying J, Bax A, (2012). Deuterium isotope shifts for backbone 1H, 15N and 13C nuclei in intrinsically disordered protein α-synuclein. J. Biomol. NMR 54, 181–191. 10.1007/s10858-012-9666-x. [PubMed: 22960996]
60. Maltsev AS & Poulsen FM (n.d.). Poulsen IDP/IUP random coil chemical shifts https://spin.niddk.nih.gov/bax/nmrserver/Poulsen_rc_CS/ (accessed May 18, 2021).
61. Williamson MP, (2013). Using chemical shift perturbation to characterise ligand binding. Prog. Nucl. Magn. Reson. Spectrosc 73, 1–16. 10.1016/J.PNMRS.2013.02.001. [PubMed: 23962882]
62. Palmer Lab | Biochemistry and Molecular Biophysics, (n. d.). https://www.biochem.cumc.columbia.edu/research-labs/palmer-lab (accessed July 16, 2021).
63. Acosta D, Das T, Eliezer D, (2020). Probing IDP interactions with membranes by fluorescence spectroscopy. In: Methods Mol. Biol. Humana Press Inc., pp. 555–567. 10.1007/978-1-0716-0524-0_28.
64. Moon CP, Fleming KG, (2011). Using tryptophan fluorescence to measure the stability of membrane proteins folded in liposomes. In: Methods Enzymol. Academic Press Inc., pp. 189–211. 10.1016/B978-0-12-381268-1.00018-5.
65. Srivastava M, Freed JH, (2019). Singular value decomposition method to determine distance distributions in pulsed dipolar electron spin resonance: II. estimating uncertainty. J. Phys. Chem. A 123, 359–370. 10.1021/ACS.JPCA.8B07673. [PubMed: 30525624]
66. Zdanowicz R, Kreutzberger A, Liang B, Kiessling V, Tamm LK, Cafiso DS, (2017). Complexin binding to membranes and acceptor t-SNAREs explains its clamping effect on fusion. Biophysical J 113, 1235–1250. 10.1016/j.bpj.2017.04.002.

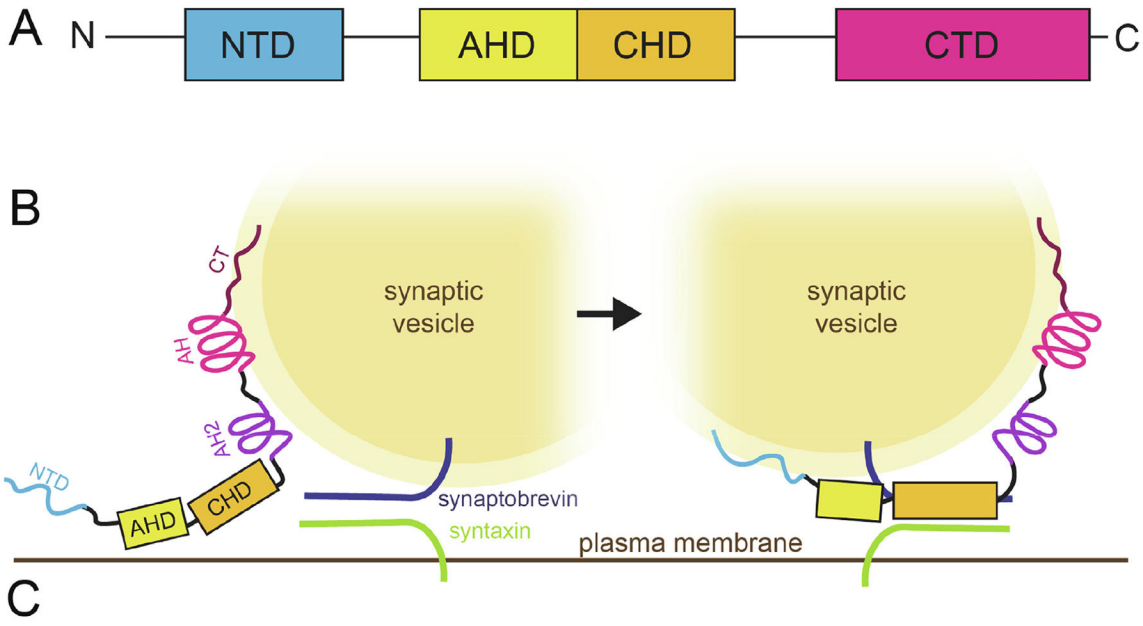

Figure 1. The complexin CTD is essential for complexin regulation of SNARE-mediated exocytosis.

(A) Complexin is comprised of four domains, all of which play specific roles in the function of the protein. (B) Through its interactions with and ability to preferentially bind highly curved membranes, the CTD is thought to tether complexin to synaptic vesicles (left) to facilitate its regulatory interactions with the SNARE complex (right). The CTD has been shown to have sub-domains that facilitate its interactions with highly-curved vesicles. Previous structural characterizations of worm complexin 1 (wCpx1) indicate that an amphipathic helix (AH) forms in the presence of highly curved vesicles, while the C-terminal (CT) motif also binds to vesicles but remains unstructured. A second amphipathic helix (AH2) retains structure even in the absence of vesicles. (C) The sequences of the CTDs of worm complexin 1 (above) and mouse complexin 1 (below) reveal little or no conservation between the two, but putative AH- and CT-motifs have been identified in the mCpx1 CTD (underlined), in analogy to the motifs previously characterized for the worm protein (bold).[34,41]

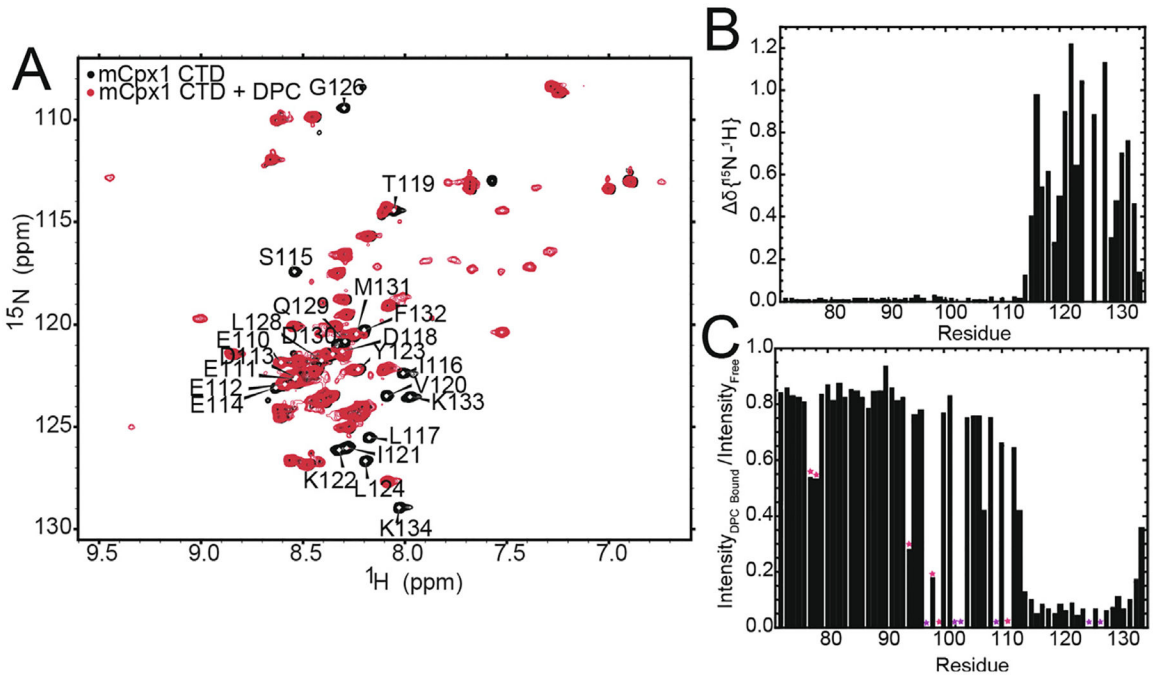

Figure 2. NMR spectra of mCpx1 CTD exhibit changes for the terminal 20 residues in the presence of DPC micelles.

(A) Clear differences in the C-terminus of the mCpx1 CTD are evident in 2D {^{15}N-^{1}H} HSQC spectra in the absence (black) and presence (red) of DPC micelles. Spectra were collected with 200 μM ^{15}N-labeled mCpx1 CTD in the absence or presence of 71 mM DPC micelles at 600 MHz (^{1}H) at 10 °C. (B) Chemical shift perturbation (CSP) plots for free vs micelle-bound mCpx1 CTD emphasize that the C-terminal ~ 20 residues constitute the only region of the protein with significant changes. (C) In addition to a global decrease in resonance intensity for the micelle-bound mCpx1 CTD, the C-terminal ~ 20 residues show greater intensity decreases. Residues with significant degeneracy impacting the intensity ratio are indicated by pink stars and prolines are indicated by purple stars.

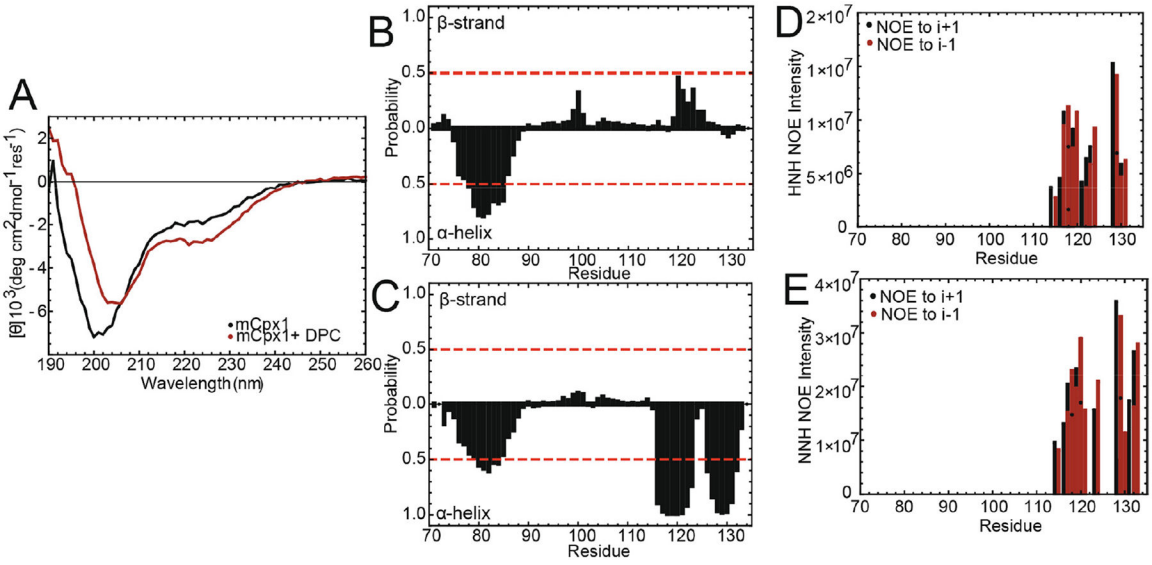

Figure 3. The mCpx1 CTD forms helical structure in both the AH- and CT-motifs in the presence of DPC-micelles.

(A) CD spectra of free mCpx1 CTD (black, 90 μM) and mCpx1 CTD in the presence of 65 mM DPC (red) indicate that the micelle-bound CTD has a higher helical content than the free protein, with shifts in signal near 208 nm and 220 nm consistent with an increase in helical structure. (B) TALOS-N predicts helical structure near the N-terminus of free mCpx1 CTD, indicating a motif corresponding to the AH2-motif previously observed for worm complexin 1. There is a region with slight propensity for beta-strand secondary structure for residues 120–124. (C) TALOS-N predicts the formation of two helical regions in the CTD in addition to the helical AH2 region in the presence of DPC-micelles. These helices correspond to the putative AH- and CT-motifs. Clear NOEs between i and i ± 1 residues are present in (D) {^{1}H-^{15}N-^{1}H} NOESY and (E) {^{15}N-^{15}N-^{1}H} NOESY spectra for the micelle-bound mCpx1 CTD from residues 113–124 and 128–133, consistent with expected NOEs for α-helices.

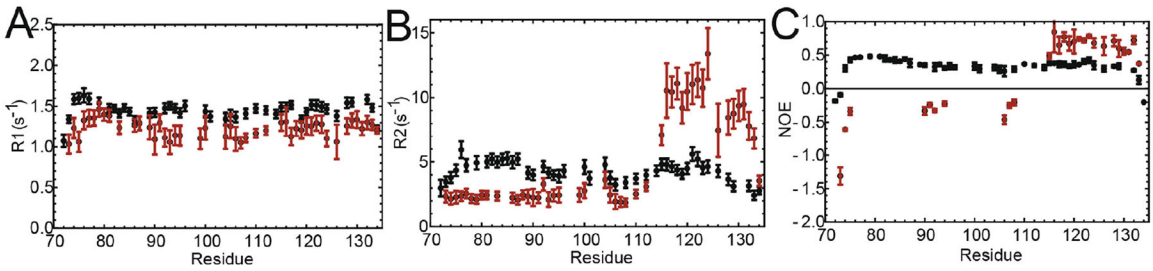

Figure 4. The mCpx1 CTD forms helical structure in both the AH- and CT-motifs in the presence of DPC-micelles.

(A) R_1, (B) R_2, and (C) heteronuclear NOE data for free (black, 10 °C) and DPC micelle-bound (red, 40 °C) mCpx1 CTD collected at 800 MHz (^{1}H) are consistent with increased rigidity in the terminal 20 residues of the protein in the presence of micelles.

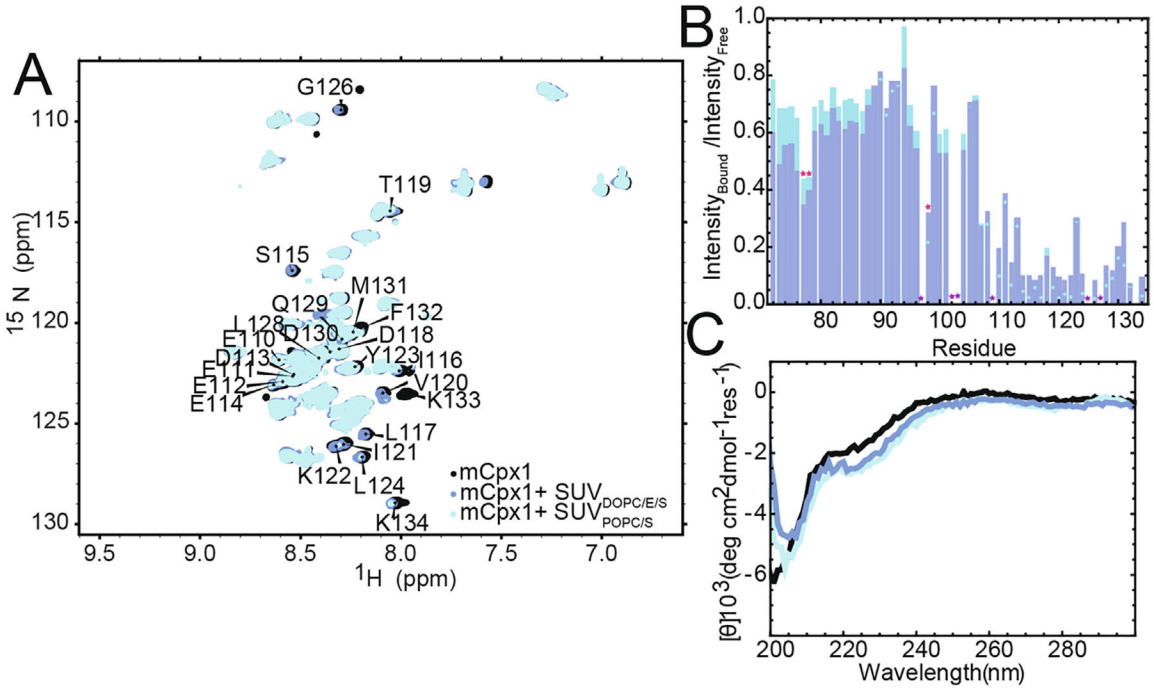

Figure 5. The C-terminus of the mCpx1 CTD interacts with SUVs.

(A) 2D {^{15}N-^{1}H} HSQC spectra reveal significant changes in the C-terminal region of the mCpx1 CTD in the presence of 10 mM 60% DOPC/25% DOPE/15% DOPS (blue) and 10 mM 85% POPC/15% POPS (cyan) relative to the free protein (black). All spectra were collected using 200 μM protein at 600 MHz (^{1}H) at 10 °C. (B) Peak intensities of SUV-bound mCpx1 CTD were specifically attenuated for the ~ 20C-terminal residues of the protein in the presence of both vesicle compositions, consistent with the effects seen in DPC-micelle bound spectra. Smaller changes are also evident near the N-terminus. Residues with significant degeneracy impacting the intensity ratio are indicated by pink stars and prolines are indicated by purple stars. (C) CD spectra for the mCpx1 CTD in the absence (black) and presence of either 10 mM 60% DOPC/25% DOPE/15% DOPS (blue) and 10 mM 85% POPC/15% POPS (cyan) indicate the formation of additional helical structure in the presence of SUVs, with alterations in signal near 208 and 220 nm consistent with a shift from random coil structure to helical structure.

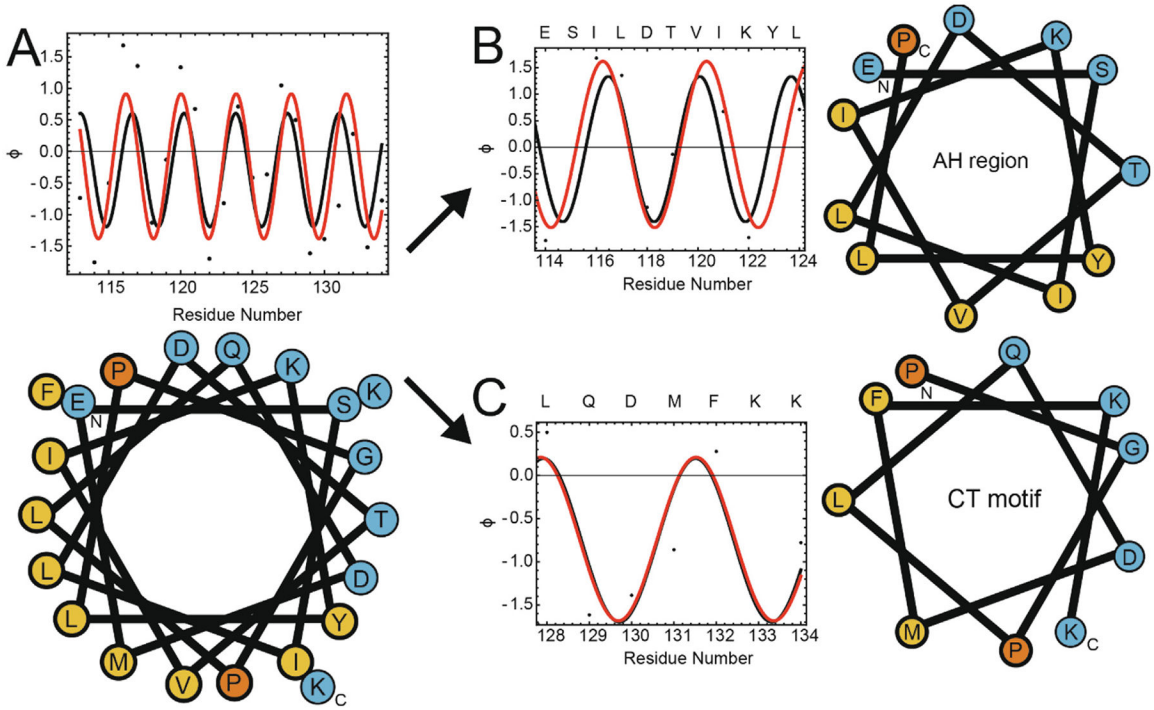

Figure 6. Power saturation continuous wave ESR data are consistent with the formation of two helical structures in the CTD in the presence of SUVs.

(A) Power saturation continuous wave ESR analysis of residues 113–134 of mCpx1 CTD are consistent with α-helical structure. The insertion depth parameter, Φ, is shown for individual residues in the CTD labeled with MTSL and indicates the ratio of accessibility for that residue to O_2 or NiEDDA ($\Phi = \ln(\Pi_{O2}/\Pi_{NiEDDA})$, with higher values indicating greater partitioning to the membrane. Sine function fits are shown using either a fixed periodicity of 3.6, characterstic of ideal α-helical structure (black, $R^2 = 0.41$) or a floating periodicity (red, periodicity 3.84, $R^2 = 0.61$). Helical wheel representations of the last 20 amino acids of the CTD partitions the nonpolar residues (yellow) from the polar and charged residues (blue), with a hydrophobic face of the helix flanked by prolines (orange), although a few polar and apolar residues cross the boundary. (B) Sine function fits to the AH-motif alone (residues 114–124) using a fixed periodicity of 3.6 (black, $R^2 = 0.64$) or allowing the periodicity to float (red: periodicity = 4.09, $R^2 = 0.90$) give improved R^2 values, and constraining the helical wheel representation to the AH-motif region alone generates a well-defined hydrophobic face. (C) Similar fits of the CT-motif alone (residues 128–134) using a fixed periodicity of 3.6 (black, $R^2 = 0.86$) or allowing it to float (red, periodicity = 3.67, $R^2 = 0.86$) also yield improved R^2 values and this region also produces an amphipathic helical wheel plot.

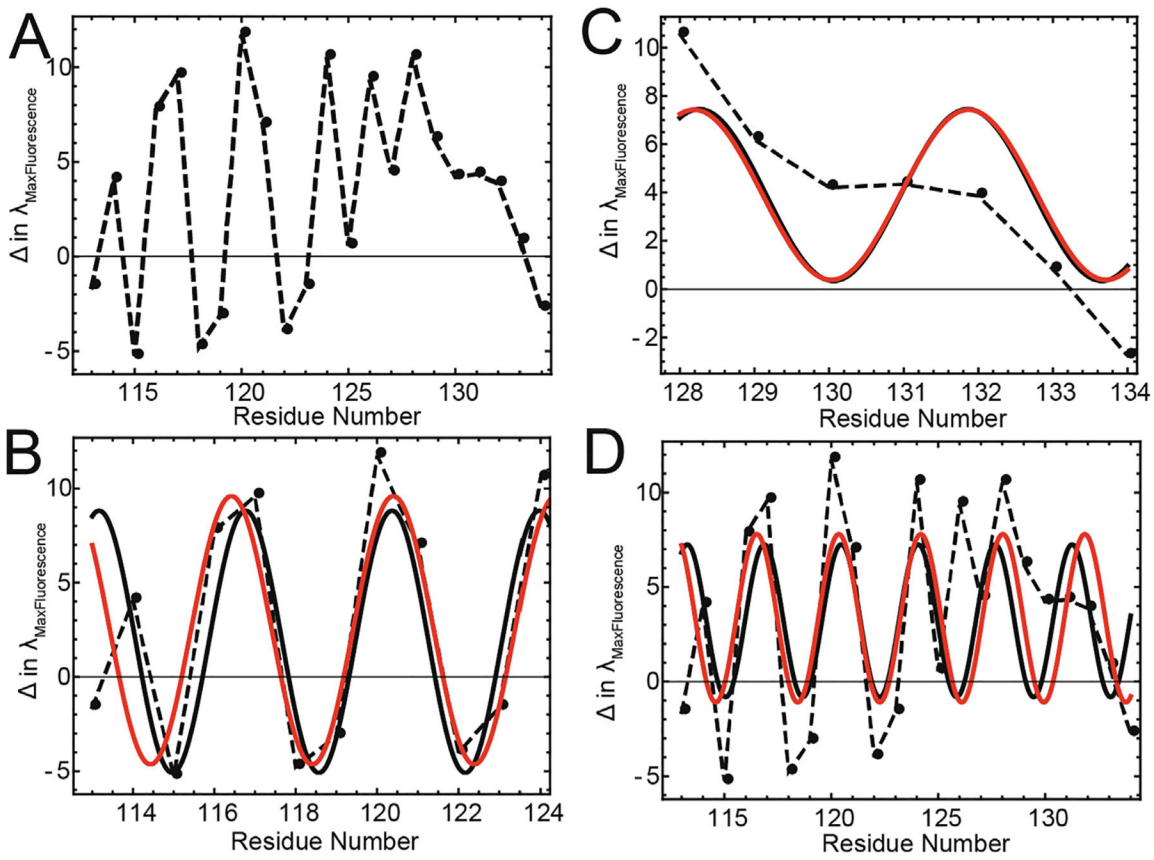

Figure 7. Trp-fluorescence captures membrane interactions of the mCpx1 CTD

(A) Shift in maximum fluorescence (Max Fluorescence Free – Max Fluorescence SUV-bound) for the mCpx1 CTD shows a clear periodicity, particularly for residues 115–125, suggesting that the Trp fluorescence captures the partitioning of residues into membrane or solvent. Data are shown for a representative dataset using SUVs composed of 85% POPC/15 %POPS. (B) The combined data sets for the AH-motif are well fit to helical structure (red: floating periodicity = 3.98, R^2 = 0.69, black: fixed periodicity = 3.6, R^2 = 0.67), as are the data for the CT-motif (C) (red: floating periodicity = 3.68, R^2 = 0.76, black: fixed periodicity = 3.6, R^2 = 0.76). (D) The data for the entire AH- and CT-motif region are not fit as well using a continuous helical structure (red: floating periodicity = 3.83, R^2 = 0.50, black: fixed periodicity = 3.6, R^2 = 0.43).

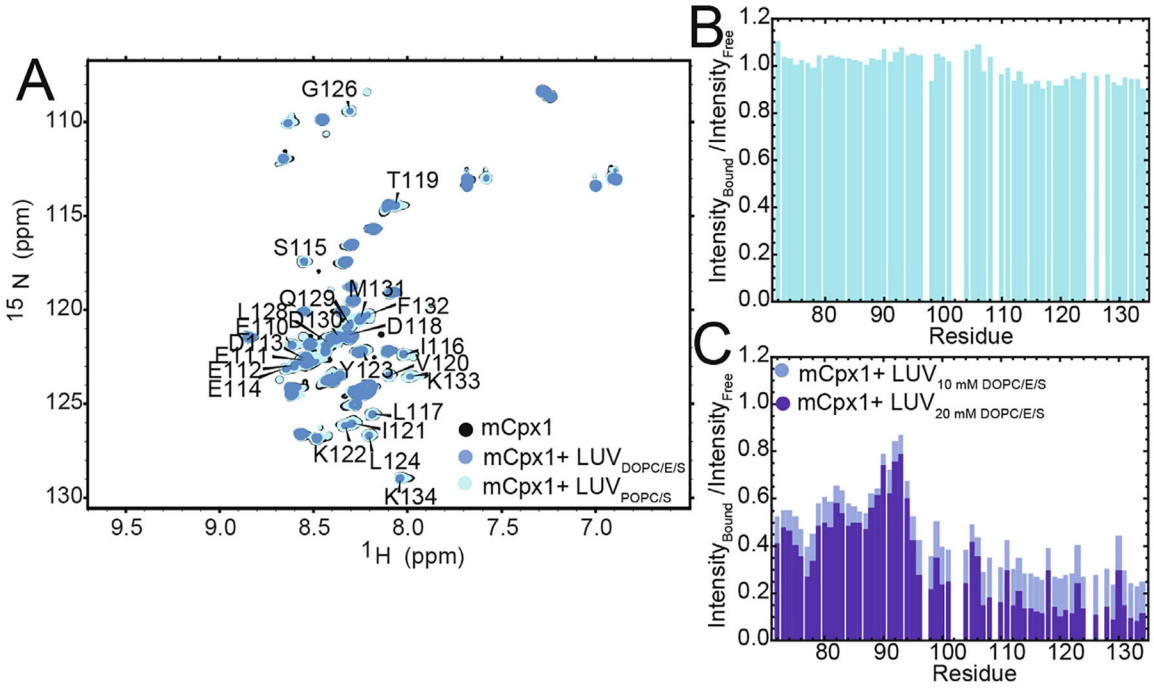

Figure 8. Interactions between mCpx1 CTD and LUVs depend on lipid composition

(A) 2D {^{15}N-^{1}H} HSQC spectrum of the mCpx1 CTD in the presence of LUVs composed of 85% POPC/15% POPS (cyan) did not reveal discernable differences relative to the mCpx1 CTD in the absence of any lipids (black). In contrast, in the presence of LUVs composed of 60% DOPC/25% DOPE/15% DOPS (blue) there is a significant attenuation of peak intensities, particularly for peaks corresponding to residues near the C-terminus of the mCpx1 CTD. Spectra were collected with 200 μM ^{15}N-labeled mCpx1 CTD in the absence or presence of 20 mM 85% POPC/15% POPS (cyan) or 20 mM 60% DOPC/25% DOPE/15% DOPS (blue) at 600 MHz (^{1}H) at 10 °C. (B) Small differences in peak intensity ratio are observed for the C-terminal ~ 20 residues of mCpx1 CTD bound to LUVs composed of 85% POPC/15% POPS relative to the free protein, indicating a weak interaction in this region. (C) Peak intensities of mCpx1 CTD in the presence of LUVs composed of 60% DOPC/25% DOPE/15% DOPS are significantly attenuated relative to the free protein for nearly all residues. In the presence of either 20 mM (lighter blue) or 10 mM (darker blue) 60% DOPC/25% DOPE/15% DOPS LUVs, there is both a global decrease in peak heights, as well as a specific attenuation of signal in the C-terminus of the protein that is concentration dependent. Interestingly, there is also a significant reduction in peak heights in the AH2 region, suggesting a possible interaction between this region and the LUVs.

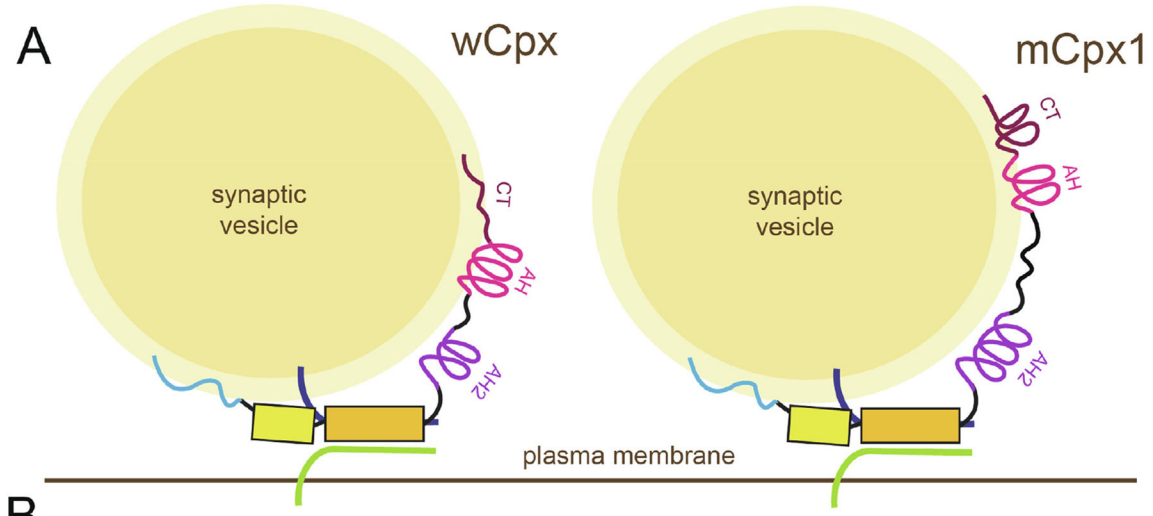

B

```
CPLX1_CAEEL    AIKKKEEGVAMDFTEGRIGGPRKTPEEIAAEMNAEDDSLIGQLGLTEQVEKAKTMATGAFETVKGFFPFGK
CPLX_DROME_A   NIKKKEEIVEAAPQEEPNPLMRKKKTPEELAAEAEQEELDDFTKLKNQIETQVNELKTQIEGKCVMQ
CPLX_DROME_B   NIKKKEEIVEAAPQEEPNPLMRKKKTPEELAAEAEQEELDDFTTKLKKRLSDAFKNCPLRNLF
CPLX1_MOUSE    GIKKKEEREAEAQAAMEANSEGSLTRPKKAIPPGCGDEPEEEDESILDTVIKYLPGPLQDMFKK
CPLX2_MOUSE    GLKKKEEKEAEEKAALEQPCEGSLTRPKKAIPAGCGDEEEEEEESILDTVLKYLPGPLQDMFKK
CPLX3_MOUSE    NETDESQIQLAGGDVELPRELAKMIEEDTEEEEDKASVLGQLASLPGLDLSSLKDKAQTTLGDLKQSAEKCHIM
CPLX4_MOUSE    SEMDETQIQLAGDDVDLPEDLRKMVDEDQDEEEEKDSILGQLQNLQNMDLDTIKEKAQATFTEIKQSAEQKCSVM
```

Figure 9. The CTD of mCpx1 is structurally distinct from the CTD of wCpx1.

(A) In the absence of highly curved membranes, both the wCpx1 and the mCpx1 CTDs are largely disordered, though both feature a helical AH2-motif, which is longer in mCpx1. In the presence of micelles, both wCpx1 and mCpx1 CTDs form helical AH-motifs. This structure is shorter in the mCpx1 CTD and is separated from the AH2 region by a longer sequence of amino acids. The CT-motif in wCpx1 remains disordered when it binds to membranes. In contrast, the CT-motif of the mCpx1 CTD adopts helical structure in the presence of membranes. It is also possible that the AH- and CT-motifs of mCpx1 may form a single functional unit that corresponds to the wCpx1 AH-motif, and that mCpx1 does not contain a functional equivalent of the wCpx1 CT-motif. (B) There are both differences and similarities between the sequences of complexin CTDs across evolutionary space. An AH-motif (pink where confirmed, underlined where predicted) appears to be conserved in many species, while the presence of AH2- (purple) and CT-motifs (maroon) are less clear.[36,38] The presence of CAAX-box farnesylation motifs (e.g. fly complexin 7A and mouse complexin 3 and 4) may offer an alternative to the wCpx1 CT-motif and suggests sub-families in which conservation between different isoforms remains to be more carefully explored.